Wideband on-chip terahertz spectrometer based on a superconducting filterbank

Akira Endo[a,b,*], **Kenichi Karatsu**[c,a], **Alejandro Pascual Laguna**[c,a], **Behnam Mirzaei**[b], **Robert Huiting**[c], **David J. Thoen**[a,b], **Vignesh Murugesan**[c], **Stephen J. C. Yates**[d], **Juan Bueno**[c], **Nuri van Marrewijk**[a], **Sjoerd Bosma**[a], **Ozan Yurduseven**[a], **Nuria Llombart**[a], **Junya Suzuki**[e], **Masato Naruse**[f], **Pieter J. de Visser**[c], **Paul P. van der Werf**[g], **Teun M. Klapwijk** [h], **Jochem J. A. Baselmans**[c, a]

[a]Faculty of Electrical Engineering, Mathematics and Computer Science, Delft University of Technology, Mekelweg 4, 2628 CD Delft, the Netherlands.
[b]Kavli Institute of NanoScience, Faculty of Applied Sciences, Delft University of Technology, Lorentzweg 1, 2628 CJ Delft, The Netherlands.
[c]SRON—Netherlands Institute for Space Research, Sorbonnelaan 2, 3584 CA Utrecht, The Netherlands.
[d]SRON—Netherlands Institute for Space Research, Landleven 12, 9747 AD Groningen, The Netherlands.
[e]High Energy Accelerator Research Organization (KEK), 1-1 Oho, Tsukuba, Ibaraki, 305-0801, Japan.
[f]Graduate School of Science and Engineering, Saitama University, 255, Shimo-okubo, Sakura, Saitama 338-8570, Japan.
[g]Leiden Observatory, Leiden University, PO Box 9513, NL-2300 RA Leiden, The Netherlands.
[h]Physics Department, Moscow State Pedagogical University, 119991 Moscow, Russia.

Abstract. Terahertz spectrometers with a wide instantaneous frequency coverage for passive remote sensing are enormously attractive for many terahertz applications, such as astronomy, atmospheric science and security. Here we demonstrate a wide-band terahertz spectrometer based on a single superconducting chip. The chip consists of an antenna coupled to a transmission line filterbank, with a microwave kinetic inductance detector behind each filter. Using frequency division multiplexing, all detectors are read-out simultaneously creating a wide-band spectrometer with an instantaneous bandwidth of 45 GHz centered around 350 GHz. The spectrometer has a spectral resolution of $F/\Delta F = 380$ and reaches photon-noise limited sensitivity. We discuss the chip design and fabrication, as well as the system integration and testing. We confirm full system operation by the detection of an emission line spectrum of methanol gas. The proposed concept allows for spectroscopic radiation detection over large bandwidths and resolutions up to $F/\Delta F \sim 1000$, all using a chip area of a few cm^2. This will allow the construction of medium resolution imaging spectrometers with unprecedented speed and sensitivity.

*Akira Endo, a.endo@tudelft.nl

1 Introduction

Cool gas is the most abundant phase of matter in the interstellar medium of galaxies, and in the Earth's atmosphere. Hence, precise knowledge of the spatial variation and dynamics of the physical and chemical properties of cool gas is of crucial importance for astrophysics,[1] as well as weather forecasting and global climate modelling.[2,3] These properties can be diagnosed using passive terahertz remote sensing, because many molecules and atoms in cool gas make energy level transitions that leave distinct fingerprints in the terahertz emission spectrum.[4] However, most of the currently used *coherent* receivers[5] can observe only $\sim$1–10 GHz of bandwidth at a time (exceptionally up to $\sim$35 GHz[6,7]). This makes it very time consuming to cover a significant fraction of the 0.1–1 THz band (referred to as 'terahertz radiation' in the remainder of this article), where the atmosphere is partially transparent. Indeed, it is often essential to probe multiple energy transitions
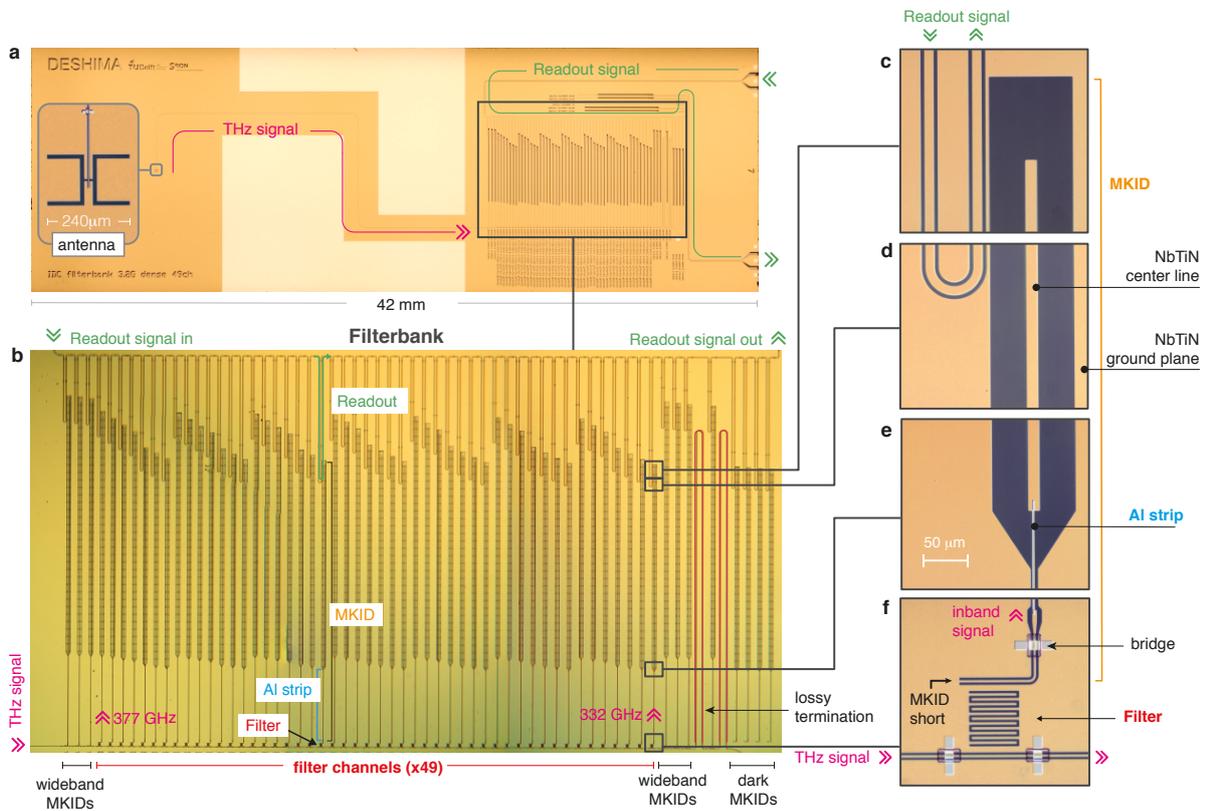
Fig 1 Filterbank spectrometer chip. a, Micrograph of the entire spectrometer chip, which has dimensions of 42 mm × 14 mm. **b**, Close-up view of the filterbank circuit. The spectral channels are placed in decreasing order of frequency, from maximum (377 GHz) to minimum (332 GHz). At the top left and right corners of the filterbank are the input and output ports of the microwave readout signals, respectively. **c–f,** Further close-up view of one of the spectral channels of the filterbank. The filter (**f**) is an interdigitated pattern etched in NbTiN, acting as a resonant bandpass filter. On both sides of the filter, the ground planes of the terahertz line are shorted with aluminium bridges over a block of UV-patterned polyimide. A bridge is also placed on the NbTiN CPW coupler of the MKID. Every MKID (**c–f**) consists of an end-shorted NbTiN CPW that couples to the filter (**f**), a narrow CPW with an aluminium center line(**e, f**), and an open-ended wide NbTiN CPW (**c–e**). The MKID is coupled to the microwave readout line near the open end (**c, d**).

of multiple chemical species to make a meaningful diagnosis, calling for much wider simultaneous bandwidths.[2,8]

The on-chip filterbank spectrometer[9–12] is a recently proposed concept that aims to enable wide-band terahertz remote-sensing spectroscopy with a threefold advance. The first step is to use an array of *incoherent* detectors[8] to measure the signal, after dispersion, in one detector for each frequency bin. This decouples the observation bandwidth from the detector readout bandwidth, allowing very efficient back-ends for medium resolution spectroscopy. The second step is to use superconducting millimeter wave electronics to: i) couple the signal to the chip, ii) to disperse it and iii) to measure it. This integrates the functionality of a classical dispersion spectrometer[8] with a typical size of ≤ 1 m onto a chip of a few cm^2, which makes the spectrometer much more scalable towards larger bandwidths, longer wavelengths, and a larger number of spectrometers to form a spectral-imaging array. The emergence of such a passive spectroscopic imager could also reform the landscape of terahertz applications in our daily lives, because it combines the advantages of a broad input frequency band, ideally suited for pressure broadened lines, fast imaging without scanning, real-time material diagnosis even through clothing, and not irradiating the subject.[13–16] The last advance is the fact that incoherent detectors allow for extremely sensitive spectroeters, especially for low radiation environments, because they are not subject to quantum noise.[8]

Here we demonstrate the design, performance and operation of the first terahertz on-chip filterbank spectrometer system, consisting of a spectrometer chip, cryogenic system and readout electronics. The spectrometer chip, as shown in Fig. 1, covers a frequency band of 332–377 GHz with 49 spectral channels with a constant spectral resolving power of $F/\Delta F = 380$. It is based on incoherent NbTiN-Al hybrid microwave kinetic inductance detector (MKID) technology[17] that can be scaled to the NbTiN gap frequency of ~ 1.1 THz, nearly doubling that of Nb technology[11] with a gap frequency of ~ 690 GHz. The sensitivity we demonstrate here is set by the photon noise inherent to the incoming optical signal, and by the instrument radiation coupling efficiency. Using large bandwidth antennas such as the leaky wave antenna[18] and the sinuous antenna THz,[19] input bandwidths in excess of one octave are possible (e.g., 300–900 GHz), allowing truly wideband spectroscopy with up to ~ 1000 channels per spectrometer.

2 Filterbank spectrometer chip

The chip is fabricated from a 100 nm-thick NbTiN film, which is deposited on the c-plane sapphire substrate using reactive magnetron sputtering.[20] This film has a critical temperature $T_c = 15$ K, which implies that the material is lossless up to the gap frequency $F_{gap} \sim 3.52 k_b T_c / h = 1.1$ THz. (k_b is the Boltzmann constant, and h is the Planck constant.) The chip couples to linearly polarised radiation using a double slot antenna, patterned using UV contact lithography and plasma etching in a $SF_6 + O_2$ plasma, followed by an in-situ O_2 cleaning.[21] The antenna is placed in the focus of a $\varnothing 8$ mm extended-hemispherical Si lens,[22] which is anti-reflection coated with a 130 μm-thick layer of Parylene-C.[23] The received signal is guided to the filterbank through the terahertz line: a coplanar waveguide (CPW) patterned in the NbTiN ground plane. The filterbank sorts the wideband signal into 49 sub-bands by means of narrow band pass filters. These filters are coplanar, interdigitated resonators, as shown in Fig. 1f, which are coupled to the terahertz line on one side, and to a NbTiN-Al hybrid MKID[24] on the other side. At the resonant frequency of the filter, maximum signal power is transferred from the terahertz line to the MKID. Each MKID is a CPW quarter wavelength resonator, with a resonant frequency in the order of 5 GHz.

Its open end is coupled to the readout line and its shorted end is coupled to the terahertz filter. Near the terahertz filter the MKID CPW has a central line made from 40 nm-thick aluminium with a resistivity of 0.8 $\mu\Omega\,\mathrm{cm}$ and $T_\mathrm{c} = 1.25$ K. For the signal frequencies of 332–377 GHz the aluminium acts as a radiation absorber, because $F_\mathrm{gap,Al} = 90$ GHz is smaller than the signal frequency band of the spectrometer. The radiation power absorbed creates a proportional shift in the resonant frequency of the MKID, which is read out as a change in the transmission phase of a microwave tone in the readout line that connects to all MKIDs. The ground planes of the readout line, and the terahertz line, are balanced using aluminium bridges with dielectric bricks fabricated from spin-coated polyimide LTC9505 from Fujifilm.[21] As a reference for the terahertz signal power at the input of the filterbank, three 'wideband MKIDs' are placed before the filterbank; these are MKIDs that are weakly coupled to the terahertz line directly without a filter, with a nearly constant power coupling of -27 dB over the relevant frequency range. Similarly, another three wideband MKIDs are placed after the filterbank for a reference of the power that runs through the filterbank without being drawn out by the filter channels. Furthermore, there are four 'dark MKIDs' that are placed away from the terahertz line as a reference for signal power coupled to the MKIDs by way of stray light or surface waves.[25] The chip is equipped with a mesh of 40 nm-thick β-phase Ta on its backside to reduce the propagation of stray radiation inside the chip. The terahertz signal line is terminated by a CPW with an aluminium center line, which absorbs the remaining terahertz signal after the filterbank, to prevent reflection of power that is not drawn out by the filter channels.

3 Spectrometer System

The filterbank spectrometer chip is integrated into a system, which includes the detector readout using microwave frequency division multiplexing (FDM) for simultaneously reading out all detectors, optics to couple the terahertz signal to the chip, and a refrigerator for cooling them. The spectrometer chip is mounted in a housing as displayed in Fig. 2a. The optical entrance of the chip housing is closed off above the lens with a 1 THz low-pass filter, and a 350 GHz bandpass filter with a transmission as shown later in Fig. 4e. The chip housing is mounted inside a light-tight chamber equipped with coaxial cable filter feedthroughs.[26] The chamber is cooled via copper thermal straps to 120 mK using a two-stage adiabatic demagnetisation refrigerator (ADR), connected to the 4 K stage provided by a two-stage pulse tube cooler. The chamber itself is isolated from the 4 K environment by a thermal-mechanical structure based on Vespel tubes. Both the chamber and chip housing operated at 120 mK are coated on the inside by a radiation absorber that consists of 3% by weight carbon powder mixed with Epotek 92 epoxy, in which we embed 1 mm or 0.5 mm SiC grains as diffusive scattering elements. This recipe is adapted from Ref.[27] to yield better absorption at long wavelengths and better adhesion on large surfaces. A microwave analog/digital readout system[28] and a 4 K low noise amplifier are used to read out the phase response of all of the MKIDs simultaneously. This is achieved by creating a time dependent signal that is the reverse Fourier transform of a set of single frequency tones, one for each MKID, with the addition of a few 'blind' tones used for system calibration and monitoring. These tones are sent to the chip, where radiation absorbed in an MKID modifies its associated single frequency tone. After passing through the chip the signal is amplified at 4 K using the low noise amplifier with a noise temperature of 5 K, after which it is further amplified and analyzed in the readout system. Here the change in complex transmission at each tone is obtained using an on-board fast Fourier transform (FFT) engine, and it is converted to a resonance frequency response in the post analysis to increase
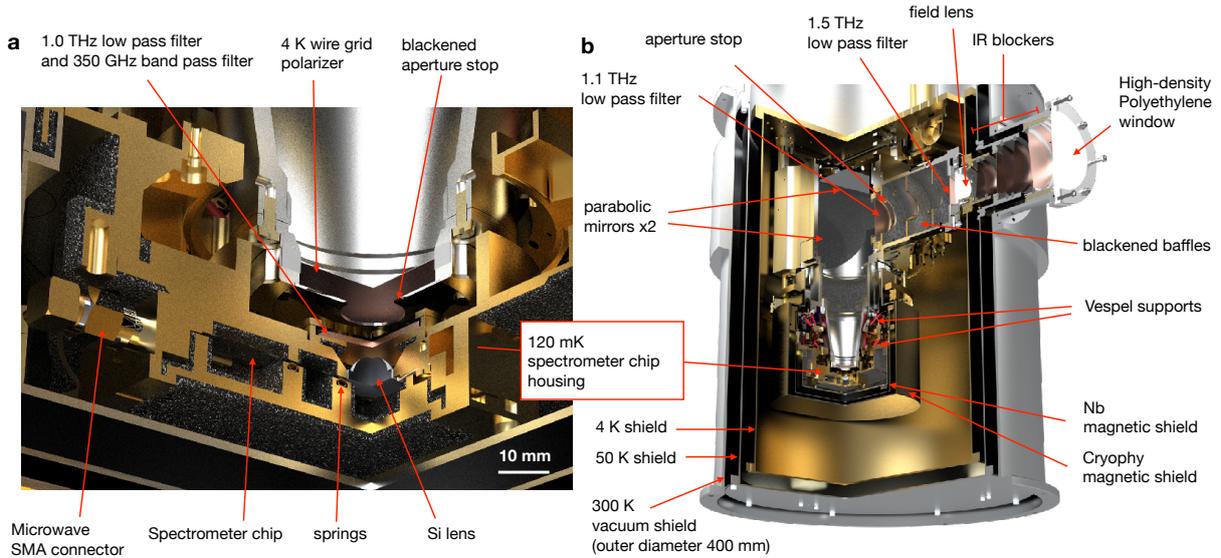
Fig 2 Cryo-optical setup of the spectrometer. a, Quarter-cutout, cross sectional view of a computer-aided drawing of the spectrometer chip mounted in a housing made of gold-plated copper. The chip is laid horizontally, with the side of the spectrometer circuit facing down. The Si lens looks into two quasioptical filters, one of which is a 1.0 THz low pass filter and the other is a 350 GHz band pass filter. The interior of the chip holder is coated with carbon loaded epoxy loaded with SiC grains.[26] The readout signal is sent in and out from the SMA connector (only one of the two is visible due to the cross-section). **b**, Quarter-cutout, cross-sectional view of the cryo-optical structure. The detector housing is placed at 120 mK, near the bottom of a double-layer cup structure made of Cryophy and Nb. The 4 K optics tube holds a wire grid, a pair of parabolic mirrors, two low pass filters, a field lens, and a pair of infrared blockers. There are also infrared blockers on the 50 K shield and 300 K shield.

the linearity.[29] Radiation is coupled to the detector chip using a 4 K light-tight box, equipped with an optical relay of two parabolic mirrors, baffling structures coated with the same radiation absorber as the 120 mK box and sample holder, infrared filters and a polarizing filter mounted in co-polarization with the antenna, as shown in Fig. 2b. The relay creates a pupil where the beam is tapered at the -10 dB level, limiting large angular stray radiation. This entire optical chain is cooled to 4 K. In addition, the chip is surrounded by two layers of magnetic shielding (Nb and Cryophy[30]), also cooled to 4 K. The combined shields attenuate the magnetic field perpendicular to the chip by a factor ~ 700.

4 Spectral response

The frequency response of the spectrometer is measured with a photomixing terahertz continuous wave (CW) source (Toptica Terabeam 1550) in a setup as shown in Fig. 3a. We couple the beam from the CW source to the cryostat by reflecting it from a 15 μm-thick sheet of Mylar to attenuate the signal power by -24 dB to -25 dB. We then measure the response of each MKID while sweeping the frequency of the CW source from 320 GHz to 380 GHz. In all results we apply a frequency shift of -0.56 GHz to the CW source frequency as a result of a frequency calibration of the CW source using a methanol emission line as will be discussed in Sec. 6.

5
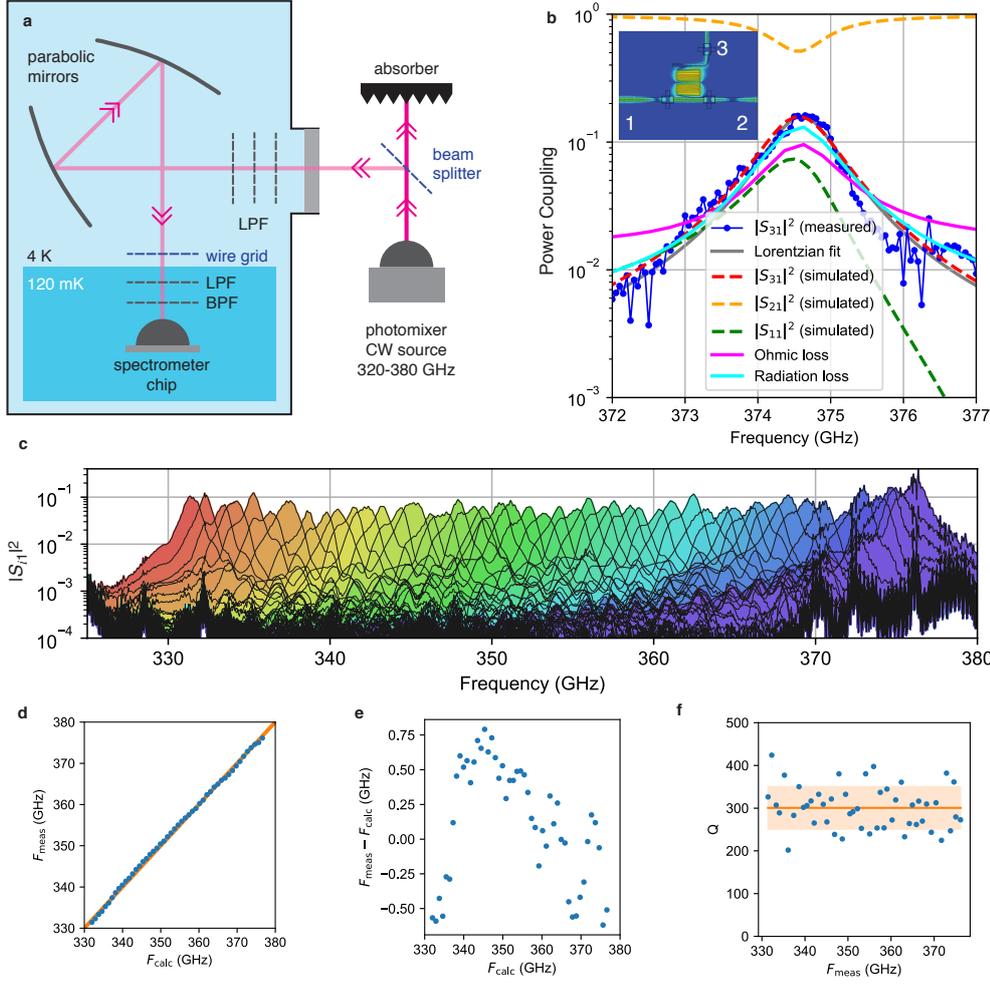
Fig 3 Terahertz frequency response of the spectrometer chip. a, The experimental configuration for measuring the frequency response. The terahertz CW signal beam from the photomixer source is reflected off a beam splitter made of a sheet of Mylar. The reflected signal enters the cryostat into the 4 K optics. The beam passes through a stack of low pass filters (LPF), two parabolic mirrors, a wire grid, and finally the 120 mK low pass filter and bandpass filter (BPF) before it reaches the spectrometer chip. **b,** The measured and simulated frequency-dependent 3-port scattering parameters. The inset shows the simulated electric field distribution $|\boldsymbol{E}|^2$ around the filter, together with the port definitions: Port 1 is the input from the terahertz through line, port 2 is the output towards the subsequent filters, and port 3 is the output towards the MKID. The plot also includes the simulated fractional power absorbed by ohmic loss in the aluminium bridges, and radiation loss into the substrate. The measured data are fitted with a Lorentzian curve, yielding a Q-factor of 361 for this filter. **c,** Measured scattering parameters $|S_{i1}|^2$ of all 49 channels ($i = 3, 4, ..., 52$), from the filterbank entrance (port 1) to the MKID. **d,** The measured peak frequency F_{meas}, determined from individual Lorentzian curve fitting, compared to an ideal geometric sequence of $F_{\mathrm{calc}} = 332 \times (1 + \Delta F/F)^i$, where the frequency spacing is $F/\Delta F = 380$ and i is the channel index. The solid line indicates $F_{\mathrm{meas}} = F_{\mathrm{calc}}$. **e,** Residual of $F_{\mathrm{meas}} - F_{\mathrm{calc}}$, plotted as a function of F_{calc}. **f,** Filter Q determined from a Lorentzian fitting to the peaks, plotted against F_{meas}. The solid line and the shaded area indicate the mean and standard deviation of Q, respectively.

Fig. 3b shows the response of one filter channel MKID near the filterbank entrance, which has less influence from neighboring channels and transmission losses compared to filters further downstream. The response plotted is normalized to the measured frequency-dependent response of a wideband MKID at the entrance of the filterbank (see Fig.1) and can be regarded as the transmission magnitude from the filterbank entrance to the MKID, which is equivalent to the magnitude of the scattering parameter $|S_{31}|^2$ according to the definition in the inset of Fig. 3b. A Lorentzian fit to the measured transmission peak yields a quality factor of $Q = 361$. The filter has a measured transmission to the MKID of $|S_{31}|^2 = 16\%$ on resonance, which is smaller than the theoretical maximum transmission of 50% for a single bandpass filter.[31] According to the power budget around the resonance frequency simulated with CST Microwave Studio[32] shown in Fig. 3b, this can be understood as a result of the following contributions: $|S_{21}|^2(\text{simulated}) = 51\%$ of the power passing through the terahertz signal line; $|S_{11}|^2(\text{simulated}) = 7\%$ being reflected back towards the input of the filterbank; 13% being lost as radiation from the filter into the substrate; and 10% being absorbed by the aluminium bridges; leaving $|S_{31}|^2(\text{simulated}) = 16\%$ to couple to the MKID, which is consistent with the measurement.

The measured transmission from the filterbank entrance to the MKIDs for all 49 channels is plotted in Fig. 3c. With $F/\Delta F = 380$ being the frequency spacing between adjacent channels, the peak frequencies of the filters follow well a geometric sequence of $F_i = 332 \times (1 + \Delta F/F)^i$ GHz, as presented in Fig. 3d. The convex trend seen in the small residual as presented in Fig. 3e is likely due to a gradient in sheet inductance of the NbTiN film along the filterbank,[20] and a scatter on the order of 0.1% of the resonance frequency as seen here is typical for MKID arrays.[22,33] In Fig. 3f we present the quality factors of all channels, showing an average $\overline{Q} = 300 \pm 50$. The frequency spacing of $F/\Delta F = 380$ is an intentional oversampling compared to the mean filter Q of 300, to conservatively avoid gaps in the spectral coverage (this resolution is well suited for the detection of redshifted emission lines from terahertz-bright galaxies[34]). As a consequence of the power being partially shared among neighboring channels, the oversampling causes the peak transmission of many channels to be slightly lower (mean of 8%) than the highest-frequency channels close to the entrance of the filterbank, such as the one shown in Fig. 3b. Collectively, the sufficiently small scatter in both filter frequency and Q makes it possible to cover the entire 332–377 GHz band without significant gaps, as demonstrated in Fig. 3c.

5 System sensitivity

Because the MKID detectors used in this study are photon-noise limited in the relevant range of terahertz loading power,[24] we can measure the sensitivity of the spectrometer by using the stream of photons as an absolute calibration source. A pair of black body radiators at room temperature $T_{\text{hot}} = 300$ K and liquid N_2 temperature $T_{\text{cold}} = 77$ K are placed at reflection and transmission positions of a wire grid seen from the spectrometer window, respectively, as shown in Fig. 4a. Looking into the wire grid, the spectrometer sees an effective load brightness temperature of $T_{\text{load}} = rT_{\text{hot}} + (1 - r)T_{\text{cold}}$, where r is the reflectance in co-polarization to the cryogenic wire grid and on-chip antenna.

Fig. 4b shows the relative frequency response $x \equiv (f_\perp - f)/f_\perp$ ($f_\perp$ is the MKID resonant frequency for $T_{\text{load}} = T_{\text{cold}}$) of a representative filter-channel MKID, as a function of T_{load}. From a square-root-law fit, we determine the temperature response $x(T_{\text{load}})$. To be able to measure

the spectrometer sensitivity expressed in noise equivalent power (NEP), we convert the load temperature to radiation power $P_{\mathrm{rad}}(T_{\mathrm{load}})$, which is defined as the single-mode, single polarization radiation power outside of the cryostat window that can couple to a single filter channel:

$$P_{\mathrm{rad}}(T_{\mathrm{load}}) = \frac{1}{2} \int_0^\infty \frac{c^2 t(F) B(F, T_{\mathrm{load}})}{F^2} dF. \qquad (1)$$

Here, $t(F)$ is the transmission of the filter channel, as shown in Fig. 3c, with the peak transmission normalized to unity. Note that we have limited the integral bounds of Eq.1 to the bandwidth of the quasioptical filter to avoid integrating noise as signal. Furthermore, c is the speed of light in vacuum, and $B(F, T_{\mathrm{load}})$ is the Planck brilliance as a function of T_{load} and frequency F. The NEP can now be determined experimentally by combining the responsivity $\frac{dx}{dP_{\mathrm{rad}}}$ with MKID photon noise level S_x using

$$\begin{aligned} NEP_{\mathrm{exp}}(T_{\mathrm{load}}) &= \sqrt{S_x} \left(\frac{dx}{dP_{\mathrm{rad}}} \right)^{-1} \\ &= \sqrt{S_x} \left(\frac{dx}{dT_{\mathrm{load}}} \right)^{-1} \left(\frac{dT_{\mathrm{load}}}{dP_{\mathrm{rad}}} \right)^{-1}, \end{aligned} \qquad (2)$$

where S_x is determined from the flat phase noise floor at >20 Hz of the power spectral density as shown in Fig 4c. The amplitude noise presented in Fig. 4c, at a level of -18 dB compared to the phase noise, corresponds to the noise in the readout system,[28] proving that the phase noise level is not affected by the readout noise. It has to be noted that both S_x and $\frac{dx}{dP_{\mathrm{rad}}}$ depend on background load P_{rad}. We plot in Fig. 4d the experimental NEP obtained using Eq. 2 at $T = T_{\mathrm{cold}}$. In the range of 345–365 GHz where the quasioptical filter stack has its highest transmission of $\sim 40\%$, the instrument has an optical NEP of $\sim 3 \times 10^{-16}$ W Hz$^{-0.5}$.

By equating the measured optical NEP to the theoretical optical NEP of photon-noise limited MKIDs[21,36] one can obtain the total coupling efficiency between the calibration load and the detector,

$$\eta_{\mathrm{opt}} = \frac{2P_{\mathrm{rad}}hF + 4\Delta P_{\mathrm{rad}}/\eta_{\mathrm{qp}}}{NEP_{\mathrm{exp}}^2 - 2P_{\mathrm{rad}}hF\tilde{n}(F,T)} \qquad (3)$$

Here, h is the Planck constant, $\tilde{n}(F,T)$ is the Boltzmann occupation number of the radiation outside of the cryostat window, and $\eta_{\mathrm{pb}} \sim 40\%$ is the pair-breaking efficiency.[37] We show the optical efficiency in Fig. 4e, together with the band-pass characteristics of the quasioptical filter stack. The figure shows that the instrument optical efficiency in the passband of the filter stack is $\eta_{\mathrm{opt}} \sim 2\%$. This is close to the product of the following transmissions: 1) Quasi-optical filter stack with a transmission of $\eta_{\mathrm{qof}} = 40\%$, 2) coupling of the cryogenic optics of $\eta_{\mathrm{co}} = 80\%$, simulated with physical optics using GRASP,[38] 3) radiation efficiency of the lens-antenna of $\eta_{\mathrm{la}} = 70\%$, simulated in CST Microwave Studio, 4) ohmic loss of the 30 bridges across the terahertz line in between the antenna and the filterbank of $\eta_{\mathrm{tl}} = 93\%$, estimated from an independent measurement of the loss of the bridges, and 5) on-chip filter has a mean peak transmission of $\sim 8\%$ as shown in Fig. 3c.

It is informative to calculate the optical efficiency for the reference MKIDs, by approximating $t(F)$ with the full passband of the quasioptical filter stack normalized to unity at the maximum. The results are shown in the right panel of Fig. 4e. The optical efficiency of the wideband MKIDs at the input of the filterbank is consistent with the designed value of -27 dB when multiplied

8
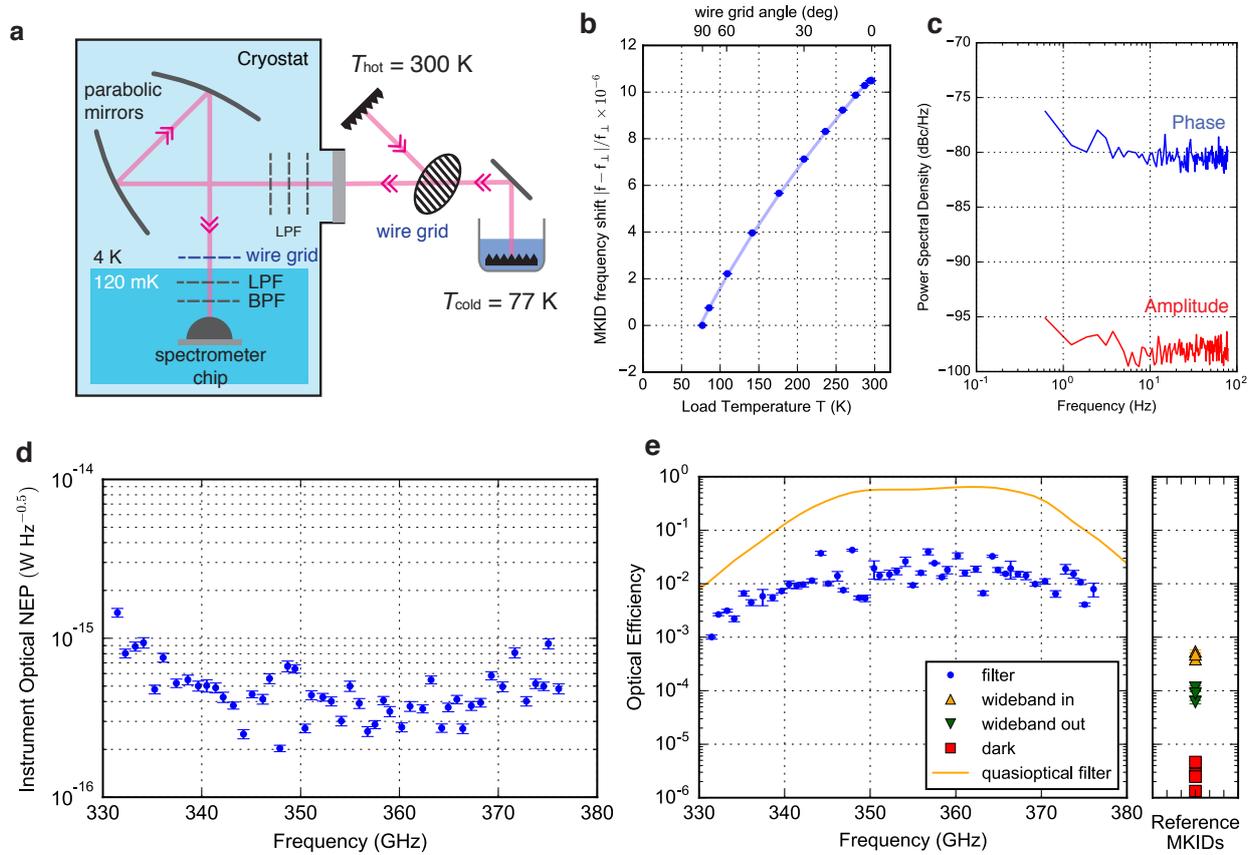
Fig 4 Instrument sensitivity of the filterbank spectrometer. a, Optical setup for characterizing the instrument sensitivity. The cryogenic wire grid transmits the linear polarization to which the antenna on the spectrometer chip is sensitive. The room temperature wire grid is rotated so that the spectrometer sees a mixture of radiation from the $T_{hot} = 300$ K black body, and the $T_{cold} = 77$ K black body immersed in liquid N_2. **b**, Response in relative MKID resonance frequency shift of one of the filterbank channels, as a function of the angle of the room temperature wire grid, and the resulting effective load temperature looking into the grid. The resonance frequency shift is measured relative to the resonance frequency ($f_\perp$) at which the wires are perpendicular to the polarization the spectrometer is sensitive to, and the spectrometer sees only the cold black body. The curve is a square-law fit to the data points. **c**, Measured phase and amplitude noise power spectral density (PSD) of a representative filterbank channel MKID, measured at minimum load temperature of $T_{load} = T_{cold} = 77$ K. Note that the spectra are taken from the signal relative to the circle traced by the frequency sweep around the resonator; see[35] for details. **d**, Optical Noise Equivalent Power for all filterbank channels as a function of filter peak frequency. The error bars (1 standard deviation) are combined statistical uncertainties from the responsivity and noise. **e**, Optical efficiency of all filter channels (left) and reference MKIDs (right, see Methods) as a function of the transmission peak frequency. The error bars (1 standard deviation) are combined statistical uncertainties from the responsivity and noise. The left panel also shows the transmission of the quasioptical filter stack as a function of frequency (solid curve).

9
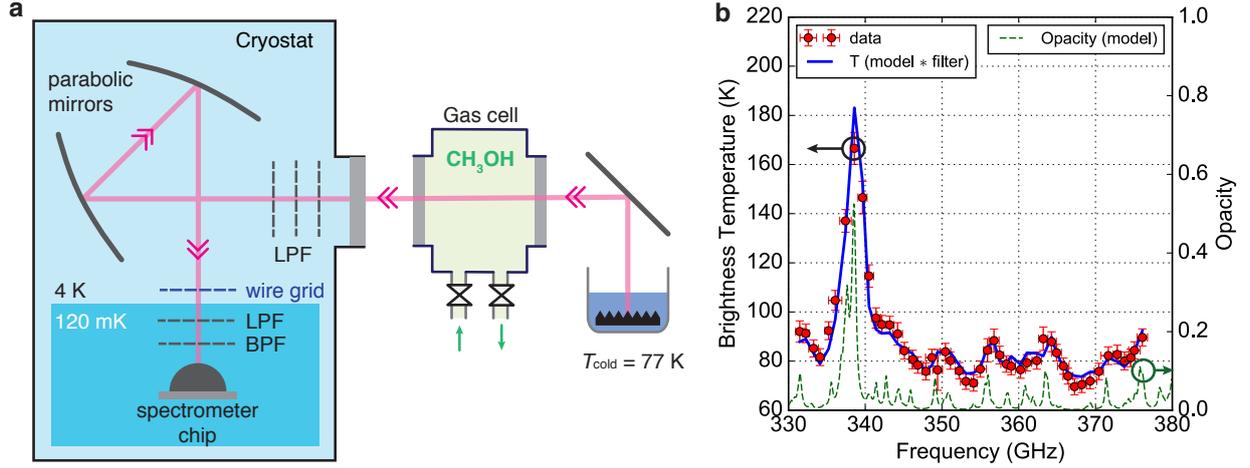
Fig 5 Detection of methanol gas with a single shot of a wideband terahertz spectrometer. a, Experimental setup. The spectrometer looks through a gas cell filled with methanol gas, into a black body load cooled with liquid N_2. **b**, Wideband emission spectrum of methanol measured with the on-chip filterbank spectrometer in a single shot. The circles indicate the brightness temperature measured using the response of the spectrometer. The dashed curve is the calculated opacity of methanol at a pressure of 17 mbar. The solid curve is the brightness temperature spectrum calculated by convoluting the model with the bandpass characteristics of the on-chip filters, with the overall amplitude and offset fitted to the measured data. The horizontal error bars represent the full width half maximum of the filter transmission of each channel. The vertical error bars represent the uncertainty in the optical spillover as estimated from the fitting in Fig. 4b.

with $\eta_{qof}\eta_{co}\eta_{la}\eta_{tl}$. The wideband MKIDs at the output of the filterbank receive less power than those at the input, because of the fraction of power taken out by the filterbank. The dark MKIDs receive 30–40 dB less power than the filter channel MKIDs, showing that the amount of stray light that couples to the MKID detectors is sufficiently small for constructing a filterbank with 10^3–10^4 channels.

6 Detection of Methanol Gas Emission Spectrum

To demonstrate that the system can spectroscopically observe emission or absorption lines from molecular gas, we have measured the emission spectrum of methanol gas at 17 mbar using the experimental configuration as shown in Fig. 5a. We couple the system beam to a gas cell that can be filled with methanol gas at 293 K so that the spectrometer looks through the gas cell into a black body cooled to 77 K with liquid N_2. Initially, the gas cell is pumped to a near vacuum of 0.014 mbar. While the spectrometer is continuously observing with all channels at a sampling rate of 160 Hz, we increase the methanol pressure to 17 mbar. The relative frequency shift $\Delta x = |f - f_0|/f_0$, where f_0 is the initial MKID frequency with the gas cell at vacuum, is converted to an effective brightness temperature T_b by using the response curve as presented in Fig. 4b for each MKID. To convert the individual filter channel response to a spectral brightness we use the measured spectral response of the filterbank, obtained using the photomixing CW source, as presented in Fig.3c. The spectral brightness obtained with our spectrometer, T_b is presented in Fig. 5b. We can compare this response to a simulation of the expected emission spectrum of methanol gas: we present the opacity of methanol gas at 17 mbar by the green dashed line in Fig. 5b. This spec-

trum is calculated using expected line frequencies and intensities from the JPL line catalog[39] and taking different line broadening mechanisms into consideration in order to comply with the length (270 mm), pressure, and temperature of the gas cell.[40] By further taking into account the losses at the gas cell window, and convoluting the spectrum with the bandpass characteristics of the filters as presented in Fig. 3c, we can calculate the expected response of each channel of the filterbank, as shown in Fig. 5b. Note that here we have applied to all of the spectral channels a common multiplication factor and an offset, to compensate for the uncertainty in the beam spillover at the windows of the gas cell and at the cold source. Interestingly, we find that we have to use an overall frequency shift of -0.56 GHz to get a maximum correspondence between the measured filterbank response and the methanol spectrum. This is consistent with the 2 GHz absolute accuracy quoted by the supplier of the CW source, and shows that it is possible to use a gas cell as a method to improve the absolute frequency calibration of the spectrometer.

From the good correspondence between measurement and simulation as shown in Fig. 5b, we can conclude that the spectral shape observed by the on-chip spectrometer reproduces very well the peak frequencies and their relative strengths expected from the database.
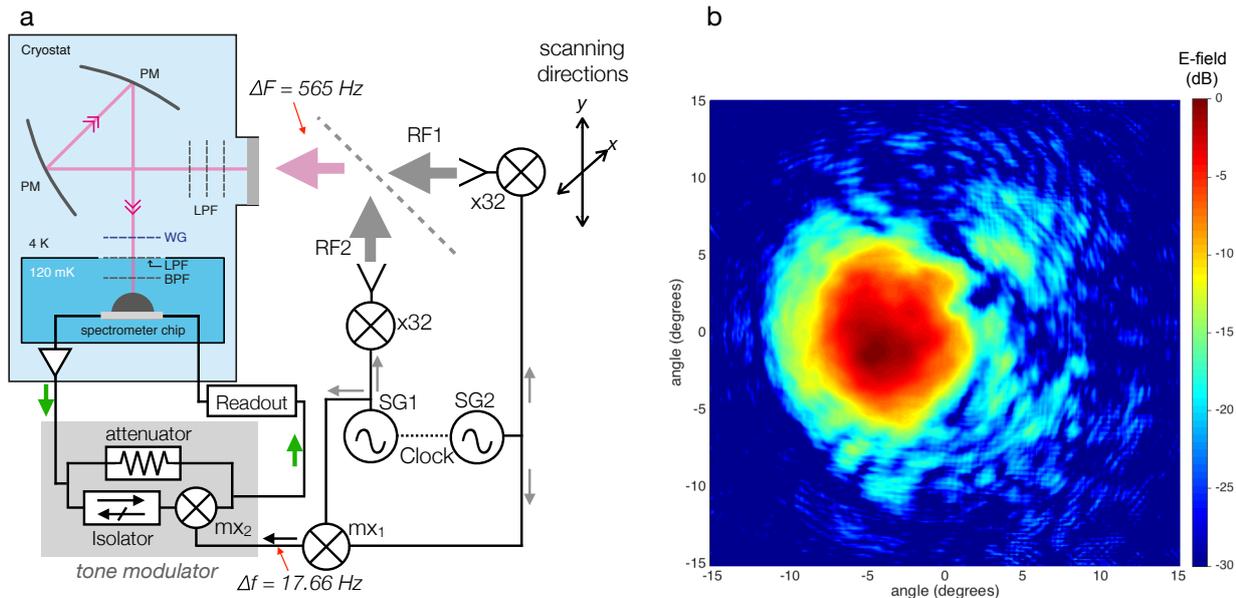
7 Measurement of the system beam pattern

The on-chip filterbank spectrometer uses direct detectors, MKIDs, but the radiation coupling via the filterbank and lens-antenna is phase coherent. The coupling between the lens-antenna and finally the telescope is sensitive to the exact phase- and amplitude distribution of the beam, details of which are easily overlooked when doing a conventional scalar beam pattern measurement using thermal sources. To avoid this, and to be able to predict the coupling to the telescope quantitatively, we have measured the phase- and amplitude pattern, using a method pioneered in Ref.[41] and explained in Fig. 6a. We use two coherent sources, each driven from a signal generator and a $\times 32$ frequency multiplier. The two synthesizers have a small frequency difference $\Delta f = 17.66$ Hz and a source offset frequency of $\Delta F = 565$ Hz, well within the bandwidth of the detectors and readout system, which modulates the detector response in the time domain. The complex field parameters can be obtained as a function of the position of RF1 by a complex FFT of the time domain data. However, MKIDs are not phase sensitive detectors and the phase information is not conserved in the detection process. To overcome this we create a stable phase reference by adding a small amplitude modulation to all the readout tones coming from the cryostat at a frequency Δf using the 'tone modulator'. The exact technique is described in great detail in Ref.[42]

We show, in Fig. 6b, the final result of this measurement, which is the far field pattern calculated from the measured data. We observe a reasonably clean pattern, which can be fitted well to a Gaussian beam, yielding a Gaussicity of 0.82, angular offsets in x and y given by $\text{off}_x = -4.0°$ and $\text{off}_y = -0.3°$, and Gaussian beam far-field divergence angle $\theta_x = 4.4°$ and $\omega_y = 5.1°$, corresponding to the $1/e^2$ value in power of the best fit Gaussian beam. The reference plane of this direction is the front side of the mounting structure of the cryostat. The cause of the relatrively large angular offset is not fully understood, but is originating at the pupil position in the cryostat.

8 Summary and Outlook

We have demonstrated the operation of a full on-chip filterbank spectrometer with 49 spectral channels with a resolution of $F/\Delta F = 380$ that observes over an instantaneous band of 332–377 GHz. The photon-noise limited sensitivity of $NEP \sim 3 \times 10^{-16}$ W Hz$^{-0.5}$, together with

11

Fig 6 The spectrometer beam pattern. a, Schematic of the beam pattern measurement setup, for more details see Ref.[42] We use 2 synthesizers at a frequency of 11.25 GHz with an offset frequency $\Delta f = 17.66$ Hz to drive two $\times 32$ multipliers, coupled to horns, to create 2 signals, one at RF1 at 360 GHz and RF2 at 360 GHz + 565.33 Hz. These are combined and coupled to the spectrometer using a beam splitter. Using mixer (mx1) we create a reference signal at a frequency Δf. This signal is fed to the 'tone modulator' indicated in the figure, which creates a small amplitude modulation on all readout signals coming from the spectrometer. This modulation creates a phase reference which allows us to obtain both the phase- and amplitude signal as a function of the position of RF1. **b**, Far field pattern in amplitude, obtained from propagating the measured pattern at the plane of RF1 to the far field.

an actual detection of methanol gas, proves that the spectrometer can already be applied in atmospheric and astronomical sciences. Indeed, the spectrometer presented here meets all the interface requirements for immediate installation on the 10 m ASTE telescope[43] as the first generation of the DESHIMA spectrometer[44] for astronomy: with the excellent atmospheric transmission of the Atacama Desert at around 350 GHz, the on-chip spectrometer will more than quadruple the simultaneous bandwidth of existing heterodyne spectrometers at this type of facilities,[45] matching well the full spectral coverage of direct-detection cameras.

Yet the system demonstrated in this Article should be regarded as a narrow-band, single-pixel demonstrator, when compared to the vast potential scalability of the on-chip filterbank spectrometer concept. By using quarter-wavelength bandpass filters[17] and wideband antennas,[18,19] the filterbank can be naturally extended to a bandwidth of 1:3 (1.5 Octave).[9] Better instrument sensitivity can be reached by increasing the system coupling efficiency, by improving the coupling efficiency of the chip and the optics. The on-chip filter transmission can be improved from ~8% to values approaching unity by a combination of two methods: First, the single filter efficiency is now limited by radiation loss and ohmic losses in the aluminium bridges. This can be mitigated by using narrower CPW filters[17] or microstrip filters,[11] and replacing the aluminium bridges with NbTiN. This will bring the single filter efficiency close to the theoretical limit of 50%.[31] The second step requires a more advanced filter design, an example would be to combine several oversampled filters to absorb more power,[31] and to incoherently couple that power into one MKID.[46] The instrument

optical efficiency can be improved by using isotropic substrates (e.g., Si) for the antenna, and by a very careful choice of the infrared and quasi-optical filters. These improvements on the chip and optics should collectively bring the instrument optical efficiency up to $\eta_{\mathrm{opt}} \sim 60\%$, corresponding to an instrument NEP of 7.9×10^{-17} W Hz$^{-0.5}$. As we show in the Appendix, an incoherent spectrometer with this NEP value will have the same per-channel sensitivity as a coherent receiver with a single-sideband receiver noise temperature of $T_{\mathrm{rx}} \sim 17$ K: this is very close to the standard quantum limit[8] of $T_{\mathrm{QN}} = h \cdot 350$ GHz$/k = 16.8$ K for coherent detection, and a factor of ~ 3 better than the state-of-the-art superconductor-insulator-superconductor (SIS) receivers for astronomy in this frequency range.[45] With the dual advantage in bandwidth and sensitivity, near-future incoherent spectrometers will offer a substantial sensitivity margin over coherent spectrometers for medium resolution spectroscopy ($F/\Delta F \leq$ a few 1000), opening up new observational parameter space in fields such as very wide-band spectroscopy and blind spectroscopic surveys.

Furthermore, the compactness of the spectrometer chip allows small spectrometer units that can be combined into a focal plane array of spectrometer pixels—what is often referred to as a hyperspectral imager or imaging spectrometer. Indeed, the on-chip spectrometer is regarded as the most viable path towards a ~ 100 pixel multi-object spectrometer, which is expected to substantially improve the galaxy-surveying capabilities of existing ground-based observatories for terahertz astronomy,[47,48] and enable future satellite missions for climatology and meteorology applications.[2]

Appendix A: Equivalent coherent receiver noise temperature of a MKID-based incoherent spectrometer

The calculation is similar to the case in which the incoherent system is completely photon-noise limited,[8] except that here we include the relatively small effect of the quasiparticle recombination noise of MKIDs. We will consider a case representative for a spectrometer system installed on a ground-based astronomical observatory, where the signal to be detected has a power that is much smaller compared to a background temperature of $T_{\mathrm{bkg}} = 77$ K typical for the 0.3–1.0 THz range.[8]

The signal to noise ratio (SNR) of a coherent receiver is given by the radiometer equation:

$$SNR_{\mathrm{coh}} = \frac{T_{\mathrm{S}}}{T_{\mathrm{N}}}\sqrt{\tau \cdot \Delta F}, \tag{4}$$

where T_{S} is the brightness temperature of the signal, T_{N} is the system noise temperature, τ is the integration time, and ΔF is the detection bandwidth. T_{N} is the sum of T_{bkg} and the receiver noise temperature T_{rx}.

Similarly, the SNR for an incoherent spectrometer is given by:

$$SNR_{\mathrm{inc}} = \frac{P_{\mathrm{S}}}{NEP}\sqrt{2\tau}, \tag{5}$$

where P_{S} is the power of the signal.

Equating $SNR_{\mathrm{coh}} = SNR_{\mathrm{inc}}$ using $P_{\mathrm{S}} \sim k \cdot \Delta F \cdot T_{\mathrm{S}}$ and $T_{\mathrm{N}} = T_{\mathrm{bkg}} + T_{\mathrm{rx}}$, we obtain

$$T_{\mathrm{RX}} = \frac{NEP}{k}\frac{1}{\sqrt{2\Delta F}} - T_{\mathrm{bkg}}. \tag{6}$$

Note that T_{RX} is independent of ΔF for a photon-noise limited MKID, because the NEP scales with $\sqrt{\Delta F}$.

As discussed in the main text, an on-chip filterbank spectrometer with an instrument optical efficiency of $\eta_{\mathrm{opt}} = 60\%$ yields a NEP of 7.9×10^{-17} W Hz$^{-0.5}$. Here we have taken $\Delta F = 0.5\pi \cdot 350$ GHz$/Q$ and $Q = 300$, where the factor 0.5π is the area under a Lorentzian curve whose peak amplitude and full-width-half-maximum are both unity. According to Eq. 6, this NEP would correspond to a T_{rx} of 17 K, which is close to the standard quantum limit for coherent detection.[8]

Disclosures

The authors have no relevant financial interests in the manuscript and no other potential conflicts of interest to disclose.

References

1 C. Kulesa, "Terahertz Spectroscopy for Astronomy: From Comets to Cosmology," *IEEE Trans. THz Sci. Technol.* **1**(1), 232–240 (2011).

2 P. Hargrave, S. Withington, S. A. Buehler, *et al.*, "THz spectroscopy of the atmosphere for climatology and meteorology applications," *Proc. SPIE* , 1021010 (2017).

3 C. Prigent, J. R. Pardo, and W. B. Rossow, "Comparisons of the millimeter and submillimeter bands for atmospheric temperature and water vapor soundings for clear and cloudy skies," *J. Appl. Meteorol. Climatol.* **45**(12), 1622–1633 (2006).

4 C. K. Walker, *Terahertz astronomy*, CRC Press, Boca Raton, 1 ed. (2015).

5 U. U. Graf, C. E. Honingh, K. Jacobs, *et al.*, "Terahertz Heterodyne Array Receivers for Astronomy," *J. Infrared Millim. Terahertz Waves* **36**, 896–921 (2015).

6 N. Erickson, G. Narayanan, R. Goeller, *et al.*, "An Ultra-Wideband Receiver and Spectrometer for 74–110 GHz," in *From Z-Machines to ALMA: (Sub)Millimeter Spectroscopy of Galaxies*, A. J. Baker, J. Glenn, A. I. Harris, *et al.*, Eds., *Astronomical Society of the Pacific Conference Series* **375**, 71 (2007).

7 R. A. Primiani, K. H. Young, A. Young, *et al.*, "SWARM: A 32 GHz Correlator and VLBI Beamformer for the Submillimeter Array," *J. Astron. Instrum.* **05**, 1641006 (2016).

8 G. J. Stacey, "THz Low Resolution Spectroscopy for Astronomy," *IEEE Trans. THz Sci. Technol.* **1**, 241–255 (2011).

9 A. Endo, P. P. van der Werf, R. M. J. Janssen, *et al.*, "Design of an Integrated Filterbank for DESHIMA: On-Chip Submillimeter Imaging Spectrograph Based on Superconducting Resonators," *J. Low Temp. Phys.* **167**, 341–346 (2012).

10 A. Endo, C. Sfiligoj, S. J. C. Yates, *et al.*, "On-chip filter bank spectroscopy at 600–700GHz using NbTiN superconducting resonators," *Appl. Phys. Lett.* **103**, 032601 (2013).

11 J. Wheeler, S. Hailey-Dunsheath, E. Shirokoff, *et al.*, "SuperSpec, The On-Chip Spectrometer: Improved NEP and Antenna Performance," *J. Low Temp. Phys.* **84**, 1–7 (2018).

12 A. Endo, "Superconducting On-Chip Spectrometery for Millimeter-submillimeter Wave Astronomy," *IEICE Trans. Electron.* **E98.C**, 219–226 (2015).

13 N. Kanda, K. Konishi, N. Nemoto, *et al.*, "Real-time broadband terahertz spectroscopic imaging by using a high-sensitivity terahertz camera," *Scientific Reports* **7**, 42540 EP (2017).

14 M. Tonouchi, "Cutting-edge terahertz technology," *Nature Photon.* **1**, 97–105 (2007).

15 S. S. Dhillon, M. S. Vitiello, E. H. Linfield, *et al.*, "The 2017 terahertz science and technology roadmap," *J. Phys. D: Appl. Phys.* **50**, 043001–50 (2017).

16 R. Appleby and R. N. Anderton, "Millimeter-Wave and Submillimeter-Wave Imaging for Security and Surveillance," *Proceedings of the IEEE* **95**, 1683–1690 (2007).

17 A. Endo, S. J. C. Yates, D. J. Thoen, *et al.*, "Superconducting Coplanar Waveguide Filters for Submillimeter Wave On-Chip Filterbank Spectrometers," *J. Low Temp. Phys.* **184**, 412–417 (2016).

18 J. Bueno, O. Yurduseven, S. J. C. Yates, *et al.*, "Full characterisation of a background limited antenna coupled KID over an octave of bandwidth for THz radiation," *Appl. Phys. Lett.* **110**, 233503 (2017).

19 R. O'Brient, P. A. R. Ade, K. Arnold, *et al.*, "A dual-polarized broadband planar antenna and channelizing filter bank for millimeter wavelengths," *Appl. Phys. Lett.* **102**, 063506–5 (2013).

20 D. J. Thoen, B. G. C. Bos, E. A. F. Haalebos, *et al.*, "Superconducting NbTiN Thin Films With Highly Uniform Properties Over a $\varnothing$ 100 mm Wafer," *IEEE Trans. Appl. Supercond.* **27**, 1–5 (2017).

21 L. Ferrari, O. Yurduseven, N. Llombart, *et al.*, "Antenna Coupled MKID Performance Verification at 850 GHz for Large Format Astrophysics Arrays," *IEEE Trans. THz Sci. Technol.* **8**(1), 127–139 (2018).

22 J. J. A. Baselmans, J. Bueno, S. J. C. Yates, *et al.*, "A kilo-pixel imaging system for future space based far-infrared observatories using microwave kinetic inductance detectors," *A&A* **601**, A89 (2017).

23 M. Ji, C. Musante, S. Yngvesson, *et al.*, "Study of Parylene as Anti-reflection Coating for Silicon Optics at THz Frequencies," in *Proceedings of the Eleventh International Symposium on Space Terahertz Technology*, 407 (2000).

24 R. M. J. Janssen, J. J. A. Baselmans, A. Endo, *et al.*, "Performance of hybrid NbTiN-Al microwave kinetic inductance detectors as direct detectors for sub-millimeter astronomy," *Proc. SPIE* **91530** (2014).

25 S. J. C. Yates, A. M. Baryshev, O. Yurduseven, *et al.*, "Surface Wave Control for Large Arrays of Microwave Kinetic Inductance Detectors," *IEEE Trans. THz Sci. Technol.* **7**, 789–799 (2017).

26 J. J. A. Baselmans, S. J. C. Yates, P. Diener, *et al.*, "Ultra Low Background Cryogenic Test Facility for Far-Infrared Radiation Detectors," *J. Low Temp. Phys.* **167**, 360–366 (2012).

27 T. O. Klaassen, M. C. Diez, C. Smorenburg, *et al.*, "Optical Characterization of Absorbing Coatings for Sub-millimeter Radiation," in *Proceedings of the Twelfth International Symposium on Space Terahertz Technology*, 400 (2001).

28 J. van Rantwijk, M. Grim, D. van Loon, *et al.*, "Multiplexed readout for 1000-pixel arrays of microwave kinetic inductance detectors," *IEEE Trans. Microw. Theory Tech* **64**, 1876–1883 (2016).

29 L. Bisigello, S. J. C. Yates, V. Murugesan, *et al.*, "Calibration Scheme for Large Kinetic Inductance Detector Arrays Based on Readout Frequency Response," *J. Low Temp. Phys.* **184**, 161–166 (2016).

30 Aperam, "Nickel Iron and Cobalt Iron Cold Rolled Strips." http://www.aperam.com/alloysandspecialities/fileadmin/pdf/Aperam/Brochure/ColdRolledStrips.pdf.

31 E. Shirokoff, P. S. Barry, C. M. Bradford, *et al.*, "MKID development for SuperSpec: an on-chip, mm-wave, filter-bank spectrometer," *Proc. SPIE* , 84520R (2012).

32 "CST Microwave Studio-3D EM simulation software." https://www.cst.com/products/cstmws.

33 C. M. McKenney, J. E. Austermann, J. Beall, *et al.*, "Tile-and-trim micro-resonator array fabrication optimized for high multiplexing factors," *ArXiv e-prints* (2018).

34 C. L. Carilli and R. Wang, "CO line width differences in early universe molecular emission-line galaxies: Submillimeter galaxies versus QSO hosts," *Astron. J.* **131**, 2763–2765 (2006).

35 J. Gao, M. Daal, J. M. Martinis, *et al.*, "A semiempirical model for two-level system noise in superconducting microresonators," *Appl. Phys. Lett.* **92**, 212504 (2008).

36 D. Flanigan, H. McCarrick, G. Jones, *et al.*, "Photon noise from chaotic and coherent millimeter-wave sources measured with horn-coupled, aluminum lumped-element kinetic inductance detectors," *Appl. Phys. Lett.* **108**, 083504 (2016).

37 T. Guruswamy, D. J. Goldie, and S. Withington, "Quasiparticle generation efficiency in superconducting thin films," *Supercond. Sci. Technol.* **27**, 055012 (2014).

38 "TICRA GRASP." https://www.ticra.com/software/grasp/.

39 R. L. Poynter and H. M. Pickett, "Submillimeter, Millimeter, and Microwave Spectral-Line Catalog," *Appl. Opt.* **24**(14), 2235–2240 (1985).

40 Y. Ren, J. N. Hovenier, R. Higgins, *et al.*, "Terahertz heterodyne spectrometer using a quantum cascade laser," *Appl. Phys. Lett.* **97**, 161105–4 (2010).

41 K. K. Davis, W. Jellema, S. J. C. Yates, *et al.*, "Proof-of-concept demonstration of vector beam pattern measurements of kinetic inductance detectors," *IEEE Transactions on Terahertz Science and Technology* **7**, 98–106 (2017).

42 K. K. Davis, S. Yates, W. Jellema, *et al.*, "Complex field mapping of large direct detector focal plane arrays," *IEEE Transactions on Terahertz Science and Technology* , 1–1 (2018).

43 H. Ezawa, K. Kohno, R. Kawabe, *et al.*, "New achievements of ASTE: the Atacama Submillimeter Telescope Experiment," *Proc. SPIE* , 701208 (2008).

44 A. Endo, J. J. A. Baselmans, P. P. van der Werf, *et al.*, "Development of DESHIMA: a redshift machine based on a superconducting on-chip filterbank," *Proc. SPIE* , 84520X (2012).

45 T. Ito, T. Kamazaki, Y. Fujii, *et al.*, "The new heterodyne receiver system for the ASTE radio telescope: three-cartridge cryostat with two cartridge-type superconducting receivers," *Proc. SPIE* , 107082V (2018).

46 O. Yurduseven, J. Bueno, S. Yates, *et al. Submitted to IEEE Trans. Terahertz Sci. Technol.* (2017).

47 D. Farrah, K. Ennico Smith, D. Ardila, *et al.*, "Review: Far-Infrared Instrumentation and Technology Development for the Next Decade," (2017).

48 R. Kawabe, K. Kohno, Y. Tamura, *et al.*, "New 50-m-class single-dish telescope: Large Submillimeter Telescope (LST)," *Proc. SPIE* , 990626 (2016).